# THz-TDS with gigahertz Yb-based dual-comb lasers: noise analysis and mitigation strategies

Benjamin Willenberg,[1,†,*] Christopher R. Phillips,[1,†] Justinas Pupeikis,[1]
Sandro L. Camenzind,[1] Lars Liebermeister,[2] Robert B. Kohlhaas,[2]
Björn Globisch,[2] and Ursula Keller[1]

[1]*Department of Physics, Institute for Quantum Electronics, ETH Zurich, Switzerland*
[2]*Fraunhofer Institute for Telecommunications, Heinrich Hertz Institute, HHI, 10587 Berlin, Germany*
[†]*These authors contributed equally to this work.*
*bwillenb@phys.ethz.ch*

We investigate terahertz time-domain spectroscopy using a low-noise dual-frequency-comb laser based on a single spatially multiplexed laser cavity. The laser cavity includes a reflective biprism, which enables generation of a pair of modelocked output pulse trains with slightly different repetition rates and highly correlated noise characteristics. These two pulse trains are used to generate the THz waves and detect them by equivalent time sampling. The laser is based on Yb:CALGO, operates at a nominal repetition rate of 1.18 GHz, and produces 110 mW per comb with 77 fs pulses around 1057 nm. We perform THz measurements with Fe-doped photoconductive antennas, operating these devices with gigahertz 1 µm lasers for the first time, to our knowledge, and obtain THz signal currents approximately as strong as those from reference measurements at 1.55 µm and 80 MHz. We investigate the influence of the laser's timing noise properties on THz measurements, showing that the laser's timing jitter is quantitatively explained by power-dependent shifts in center wavelength. We demonstrate reduction in noise by simple stabilization of the pump power and show up to 20 dB suppression in noise by the combination of shared pumping and shared cavity architecture. The laser's ultra-low-noise properties enable averaging of the THz waveform for repetition rate differences from 1 kHz to 22 kHz, resulting in a dynamic range of 55 dB when operating at 1 kHz and averaging for 2 s. We show that the obtained dynamic range is competitive and can be well explained by accounting for the measured optical delay range, integration time, as well as the measurement bandwidth dependence of the noise from transimpedance amplification. These results will help enable a new approach to high-resolution THz-TDS enabled by low-noise gigahertz dual-comb lasers. © 2024 Optica Publishing Group under the terms of the Optica Open Access Publishing Agreement

https://doi.org/10.1364/AO.522802

## 1. INTRODUCTION

The THz range is of special interest for scientific and industrial applications since it allows for non-invasive detection and analysis of many materials that are opaque in the visible and infrared [1]. Applications include detection of spectroscopic features in the 1 THz to 5 THz range to distinguish between plastics and explosives that look visibly identical [2], quality control monitoring through opaque packaging, non-invasive layer thickness measurements of paint with µm-accuracies [3], high-resolution gas spectroscopy, and alternatives to x-ray technology for label-free analysis of biological tissue (since THz radiation is non-ionizing) [4]. These applications are commonly addressed by the terahertz time-domain spectroscopy (THz-TDS) technique.

In THz-TDS, one optical pulse train generates a train of single-cycle THz pulses on an emitter device, while the other optical pulse train is delayed and equivalent time samples the THz field on a receiver device [5]. The progress in photoconductive antennas (PCAs) in the past decade has made them one of the preferred choices for table-top systems [6]. A commercially established approach is to use Fe doping to obtain ultrafast PCA device recovery and to fiber couple the devices so that they can be driven with modelocked fiber lasers operating at 1550 nm [7,8]. Alternative dopants are being actively explored to boost the efficiency even further, with conversion efficiencies as high as 3.4% shown in [9] at moderate optical pulse energies of a few hundred picojoules. As well as PCA based experiments, terahertz generation using nonlinear crystals and ≫ nJ-level optical pulse energies has also received a great deal of attention [10,11]. Advances in nonlinear optics such as difference frequency generation [12], optical parametric oscillation [13], and optical rectification [14] are also helping to bridge the gap between the THz and mid-infrared domains.

THz-TDS can be implemented with a mechanical delay stage to scan the delay and thereby sample the THz temporal waveform, but the stage imposes a severe trade-off between the speed and range of the scan. As an alternative, a pair of lasers with slightly detuned pulse repetition rates can be used to implement equivalent time sampling (ETS) [15], also referred to as asynchronous optical sampling (ASOPS) [16]. Between each subsequent pair of pulses, the optical delay changes by $1/f_{\mathrm{rep}}^{(1)} - 1/f_{\mathrm{rep}}^{(2)} \approx \Delta f_{\mathrm{rep}}/f_{\mathrm{rep}}^2$, where $f_{\mathrm{rep}}^{(j)}$ is the repetition rate of laser $j$, $\Delta f_{\mathrm{rep}}$ is the repetition rate difference, and $f_{\mathrm{rep}}$ is an average repetition rate. Therefore, an optical delay range of $1/f_{\mathrm{rep}}$ is scanned within a measurement time of $1/\Delta f_{\mathrm{rep}}$, corresponding to a large temporal stretch factor of $f_{\mathrm{rep}}/\Delta f_{\mathrm{rep}}$. Because this method of delay scanning does not require any moving parts, it is possible to obtain much faster and longer-range scans compared to conventional mechanical delay-line-based pump-probe measurements.

However, THz systems using PCAs typically use lasers with repetition rates of around 100 MHz, implying a long scan range of order 10 ns. Such a large delay range is only needed for specific applications (such as measuring targets with long response times or the sharp absorption lines of molecular gases at low pressures) [1]. For many applications a shorter range (<1 ns) and a corresponding spectral resolution (>1 GHz) are sufficient, with examples including gas spectroscopy at ambient pressures, or detection of small variations in the thickness of thin-film layers [17]. Limiting the scan to a shorter range avoids the dead time at the end of the time window, which improves the dynamic range (DR) since the signal of interest will occupy a larger fraction of the measurement window. Electronically controlled optical sampling (ECOPS) [18] and other techniques [19,20] have been developed to address this by electronically controlling the pulse-to-pulse delay over a limited range much smaller than $1/f_{\mathrm{rep}}$.

An alternative and potentially simpler approach is to use a higher pulse repetition rate. Gigahertz repetition rates enable high (multi-kHz) update rates while scanning the full delay range with ≪ 100 fs resolution. In the context of THz-TDS with PCAs, such lasers are also a promising path to boost the signal strength by using a higher average power while staying below the pulse energy damage threshold of the devices. Gigahertz lasers have been explored for pump-probe spectroscopy via Ti:sapphire lasers at 1 GHz [21] and 10 GHz [22], but the high cost of the laser technology has hindered wider adoption. One aspect of this is the cost of traditional Ti:sapphire laser systems due to their more complicated pump schemes compared to diode-pumped lasers, although there has been substantial recent progress in addressing that issue [23–26]. Another aspect relates to system complexity, since one needs a pair of lasers and ultra-precise active stabilization of $\Delta f_{\mathrm{rep}}$ to maintain calibration of the time-dependent optical delay.

Here, as an alternative to stabilized Ti:sapphire lasers and similar approaches to ETS, we explore single-cavity dual-comb lasers based on diode-pumped Yb gain media. Dual-comb lasers, which are very similar or even identical to the lasers used for ETS applications, are so named due to their connection with optical frequency comb generation [27]. Dual optical frequency combs [28,29] are an interesting extension of the optical frequency comb involving a pair of combs with a slight but well-defined difference in their comb spacing and hence pulse repetition rate. The idea of generating both combs in a single cavity has emerged as a compelling alternative to active stabilization, since a shared cavity architecture leads to correlated noise properties between the two combs while simultaneously reducing complexity of the system (one free-running laser instead of two mutually stabilized ones). This approach has been demonstrated with many laser platforms, including semiconductor disk lasers [30], free-space bidirectional ring lasers [31], bidirectionally modelocked fiber lasers [32,33], hybrid waveguide lasers [34], and other approaches [35]. Such lasers have also been applied to THz-TDS at megahertz repetition rates [36–38]. Recently, we have demonstrated a set of free-running solid-state single-cavity systems with all common optics and ultra-low relative timing noise performance utilizing birefringent multiplexing [39,40] or spatial multiplexing [41,42]. The system reported in [41] allowed for sub-cycle relative timing jitter ([20 Hz, 100 kHz] integration range) and thereby surpasses the performance of traditional ASOPS systems with two locked lasers for pump-probe measurements.

Use of gigahertz lasers for dual-comb spectroscopy and THz-TDS has seen renewed interest in recent years due to advances in high-repetition-rate ytterbium- and erbium-based frequency combs [43–47], and the advantages high pulse repetition rates offer in terms of high-speed measurements for real-time material inspection and label-free imaging. Diode-pumped solid-state lasers with low-loss, low-nonlinearity, low-dispersion cavities are ideally suited for generating gigahertz combs [48,49], and they are simpler than traditional Ti:sapphire systems while offering stronger damping of high-frequency pump intensity fluctuations. They also support lower noise [44], higher power, and exhibit more straightforward repetition rate scaling compared to fiber lasers. Yb-doped gain media also have favorable thermal properties and can be diode pumped with high efficiency and low quantum defect.

Here we study THz-TDS driven by a new Yb:CALGO-based single-cavity dual-comb laser based on operating at a gigahertz repetition rate and pumped by a single-mode (SM) laser diode. We obtain 77 fs pulses with 110 mW average power per comb at a repetition rate of 1.18 GHz and center wavelengths around 1057 nm. Our THz experiments are focused on the efficient Fe-doped photoconductive antenna devices similar to those presented in [7]. We consider three critical topics connected to THz-TDS measurements with free-running dual-comb lasers: (i) THz generation and detection (Section 2); (ii) laser timing jitter (Sections 3 and 4); and (iii) dynamic range of the THz spectrum for high-resolution spectroscopy measurements (Section 5). We show efficient generation and detection of THz radiation using Fe-doped PCA's using gigahertz Yb-based lasers for the first time, reaching parity with reference measurements performed using 1550 nm fiber lasers operating at 80 MHz. With respect to timing, we demonstrate ultra-low-noise performance of $\Delta f_{\mathrm{rep}}$, and demonstrate strong noise suppression via either introducing noise correlations or feedback stabilization of the SM pump diode. Furthermore, we show excellent quantitative agreement between the timing jitter power spectral density of the laser and theoretical calculations based on the laser's power-dependent shift in center wavelength. We carried out THz measurements at repetition rate differences

$\Delta f_{rep} \geq 1$ kHz to (i) show high update rate compatibility and (ii) maintain calibration of the timing axis subject to the small but finite jitter of the laser. We obtain a spectrum with 55 dB peak DR in a 2-s-long measurement, allowing to detect absorption features up to 3 THz. We show how the DR can be fully explained by considering the required transimpedance amplifier bandwidth. The amplifier noise is governed by the gain bandwidth required, which is determined by the ratio $\Delta f_{rep}/f_{rep}$. In turn, suitable values of $\Delta f_{rep}$ are constrained by laser timing jitter. Our results thus show how these interconnected issues can be managed to obtain practical measurements by a combination of shared cavity architecture, shared pumping, and pump stabilization. Our results should help enable a new path to THz-TDS at high repetition rates using Yb-based gigahertz dual-comb lasers.

## 2. THZ-TDS SYSTEM

The experimental setup is shown in Fig. 1. A low-noise gigahertz dual-comb laser is used to drive THz PCA devices for THz-TDS measurements. The setup also includes a dual-comb interferometry (DCI) measurement, which is used to determine when the pulses from the two combs are temporally overlapped.

### A. Dual-Comb Laser Output

The laser is a diode-pumped solid-state laser (DPSSL) that we developed for this project, based on Yb:CALGO as the gain medium. An intracavity biprism is included in the cavity in order to obtain dual-comb operation from a shared cavity arrangement, analogous to our previous demonstrations at 80 MHz and 1 GHz [41,42]. In this section we discuss the laser's output properties as they pertain to the generation and detection of THz radiation. Implementation details of the dual-comb
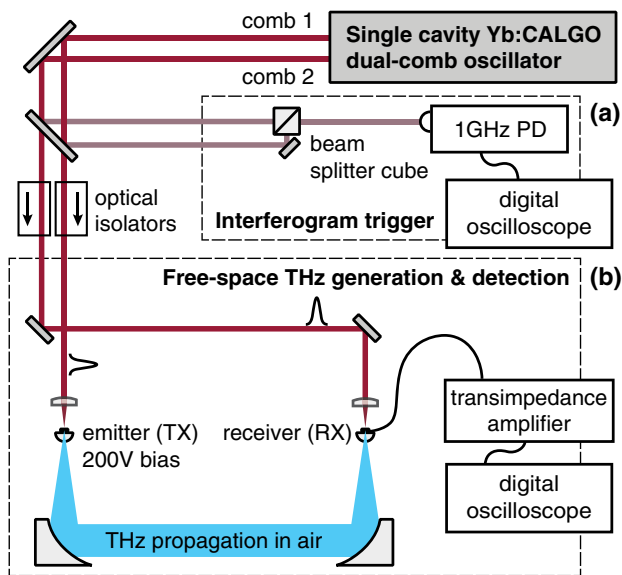


**Fig. 1.** Schematic of the setup. (a) Gigahertz dual-comb laser; laser cavity and other implementation details are discussed in Section 3.B. (b) Dual-comb interferometry setup to measure when the pulses are temporally overlapped. (c) THz time-domain spectroscopy setup with free-space photoconductive antennas for THz generation and detection.
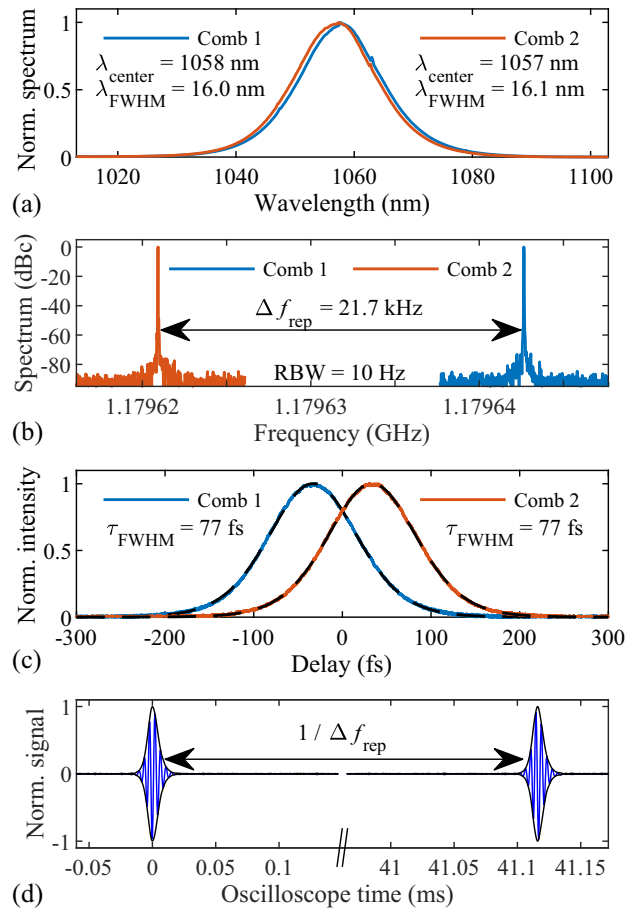


**Fig. 2.** Characterization of the dual-comb laser output with both combs operated simultaneously at maximum power. (a) Optical spectrum. (b) Pulse duration measurement via second harmonic autocorrelation. The pulse durations $\tau_{FWHM}$ are obtained via deconvolution assuming a $\text{sech}^2$ pulse shape (dashed lines correspond to $\text{sech}^2$ fit). (c) Radio frequency spectrum of each comb around the repetition rate of the oscillator at a repetition rate difference of 21.7 kHz. (d) Example interferograms measured via dual-comb interferometry setup. The dashed line indicates the envelope (magnitude of analytic signal) that is used to determine the center positions $T_n$.

laser itself are discussed in Section 3.B, and its noise properties are analyzed in Sections 3 and 4.

At the highest power operation point the average power of each comb is 110 mW, and their pulse properties are very similar. The center wavelengths are 1058 nm for comb 1 and 1057 nm for comb 2, and both spectra have a full width at half maximum (FWHM) bandwidth of 16 nm [Fig. 2(a)]. The pulse duration is 77 fs measured with second-harmonic autocorrelation [Fig. 2(b)]. We observe a clean radio frequency (RF) spectrum for both combs at a fundamental repetition rate $f_{rep} \approx 1.1796$ GHz [Fig. 2(c)]. The repetition rate difference was set to $\Delta f_{rep} = 21.7$ kHz for this measurement, but it can be tuned over a range of $\pm 175$ kHz by lateral translation of the intracavity biprism.

A small part of each comb is split off and directed towards the DCI setup in order to determine the times $T_n$ when the pulses of the two combs are perfectly temporally overlapped. When the pulses are temporally overlapped at the beam splitter they

interfere, leading to an interferogram that repeats with a period of $1/\Delta f_{\text{rep}}$. Each peak time $T_n$ is determined by a center of mass calculation on the envelope of the interferogram, as depicted in Fig. 2(d). The measured values of $T_n$ are used to infer and correct for fluctuations in $\Delta f_{\text{rep}}$, and thereby enable averaging of multiple periods of the THz-TDS signal (see Section 2.C).

### B. THz Generation and Detection

For the THz experiments we direct the light of the two combs onto two free-space photoconductive antennas produced at HHI [Fig. 1(c)]. In the active region of the emitter device, each laser pulse generates a localized charge cloud that is accelerated in the 50 µm gap between the two electrodes by the bias electric field and thereby generates pulsed THz radiation. The ultrafast trapping time of the iron-doped InGaAs material platform used for the photoconductive antenna enables short THz pulses with frequency content up to >6 THz [7]. The generated THz radiation is collimated and refocused onto the receiver device by a pair of silicon ball lenses (mounted directly to the photoconductive antennas) and metallic off-axis parabolic mirrors. In the receiver device the optical pulses from the second comb act as a gate in order to optoelectronically sample the THz wave. More specifically, each optical pulse generates a charge cloud in the 10 µm antenna gap that is accelerated by the electric field of the THz wave, thereby inducing a small electrical current in the nA–µA range, which is transimpedance amplified and detected on an oscilloscope. Voltage noise considerations relating to the detection scheme are discussed in Section 5.

To ensure no optical feedback between the THz photoconductive antennas and the laser oscillator, both free-space beam paths include a Faraday isolator (EOT, PAVOS+). The optical power in the emitter and receiver arm is controlled by a pair of half-waveplate and polarizing beam splitter. Comb 1 is focused to a sub 50 µm $1/e^2$ spot diameter on the emitter with a $f = 50$ mm aspheric lens, and comb 2 is focused to a sub 10 µm spot diameter on the receiver with a $f = 20$ mm lens. The positive dispersion added by the transmissive optics and the isolator crystal is compensated for by negative dispersion (total around $-4000$ fs$^2$) from chirped mirrors to ensure compressed <80 fs pulses on the photoconductive devices.

### C. THz Signals

To characterize the THz signal we set $\Delta f_{\text{rep}}$ to 22 kHz, and averaged over all $1/\Delta f_{\text{rep}}$ periods in a 2-s-long time trace. The averaged signal over the full delay range $1/f_{\text{rep}} \approx 850$ ps is shown in Fig. 3(a), and a zoom-in around the main peak is shown in Fig. 3(b). The bias voltage applied to the emitter was 200 V and the average optical powers reaching the emitter and receiver were 80 mW and 30 mW, respectively. Apart from the main peak, the first 50 ps of the delay range exhibits clear oscillations caused by the free induction decay of water vapor absorption in the free space THz beam path, which was approximately 30 cm. The spectroscopic aspects of these measurements are discussed further in Section 5.B. An additional peak at about 620 ps is visible in the time trace originating from an etalon effect between the emitter and receiver antenna in the THz beam path. To avoid ripples on the spectrum due to this
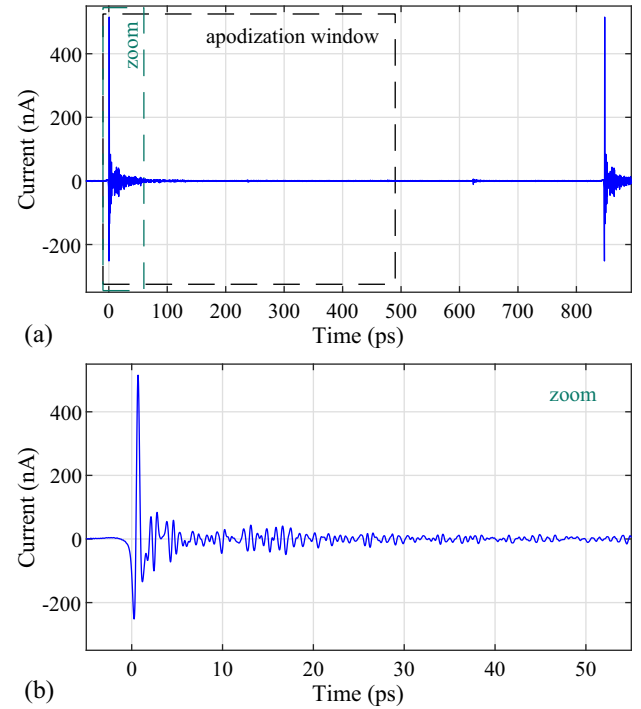


**Fig. 3.** (a) THz signal obtained after 2 s integration time or ~44000 averages for the full optical delay range of $1/f_{\text{rep}} = 850$ ps at a repetition rate difference of the dual-comb laser of ~22 kHz. (b) Zoom to the first 50 ps of the signal. Note that a digital bandpass filter has been applied that limits the signal to THz frequencies in the range [50 GHz, 5 THz].

we restrict our analysis to the first 500 ps; the corresponding apodization window is indicated in Fig. 3(a).

The averaging was performed by using the DCI measurement taken at the same time to resample the data in post processing. The corresponding IGMs provide the time stamps $T_n$ when the pulses are temporally overlapped [see Fig. 2(d)]. Resampling with such time stamps is a standard procedure, which we briefly re-iterate here in a convenient form. Consider the phase obtained by integrating the instantaneous repetition rate difference of the two combs $\Delta f_{\text{rep}}(t)$:

$$\phi_\Delta(t) = 2\pi \int_{T_0}^{t} \Delta f_{\text{rep}}(t')\mathrm{d}t'. \tag{1}$$

At the IGM peaks $T_n$, all the RF comb lines have the same phase and constructively interfere. Therefore, the phase satisfies $\phi_\Delta(T_n) = 2\pi n$ for integer $n$. We thus estimate $\phi_\Delta(t)$ by interpolation, with $\{T_n\}$ as abscissa and $\{2\pi n\}$ as ordinate. Given $\phi_\Delta(t)$, the optical delay $\tau$ as a function of measurement time $t$ can be approximated, assuming small relative changes in $f_{\text{rep}}$, by

$$\tau(t) \approx \frac{1}{\langle f_{\text{rep}}\rangle}\mathrm{mod}\left(\frac{\phi_\Delta(t)}{2\pi}, 1\right), \tag{2}$$

where we use $\langle \rangle$ when we want to explicitly emphasize a time-averaged quantity. The limitations of ETS averaging when using interpolated values of $\phi_\Delta(t)$ in Eq. (2) and how they connect with the timing noise of the dual-comb laser are discussed in Section 3.

An important aspect of our experiment is that we explore the operation of Fe-doped PCA devices using Yb laser technology for the first time. Reference measurements for comparable devices to those used in our experiment have been performed using a laser with a driving wavelength of 1550 nm and a pulse repetition rate of 80 MHz. Under these test conditions, the obtained peak THz signal current strength amounts to 500 nA to 700 nA with 20 mW of optical power on both the emitter and the receiver. Despite the drastically different configuration in our system (wavelength of 1050 nm and repetition rate of 1.2 GHz), we obtain comparable performance in the generated THz signal current (515 nA to 550 nA). In the reference measurements the pulse energy was kept low in order to avoid damage to the sensitive PCAs. In our measurements, although we use slightly higher average powers of 80 mW on the emitter and 30 mW on the receiver, this corresponds to considerably lower pulse energy due to the gigahertz repetition rate of the laser (less charge per pulse, but more pulses). One factor contributing to the increased average power needed in our experiments is the photon number scaling between a 1550 nm and 1050 nm driver. Our results highlight how gigahertz lasers offer an appealing route to scaling the THz signal strength, and compatibility with Yb technology rather than Er technology allows for more efficient and powerful lasers without requiring any amplification and with less sensitivity to thermal effects in the gain medium.

Apart from generating a strong THz signal, the timing jitter and voltage noise are two critical and connected considerations to obtain a high dynamic range. We discuss these aspects in the following sections and how they can be addressed by laser design strategies.

## 3. DUAL-COMB LASER: RELATIVE TIMING NOISE

### A. General Considerations

Excessive laser timing fluctuations cause the equivalent time sampling signal to get smeared out when the uncertainty in the delay between the two pulses reaches a small fraction of the inverse bandwidth of the signal. Accurate calibration of the optical delay $\tau(t)$ at all times $t$ in the measurement is therefore critical. Inferring $\tau(t)$ via the time stamps $T_n$ is an appealing solution to this calibration problem due its simplicity. For example, IGMs can be obtained with just a few optical components, and the time stamps could be obtained by rectifying the envelopes and measuring them with time to digital chips developed for LIDAR applications [50]. The time stamps can also be obtained by optical sum frequency mixing between the two combs (avoiding the need for rectification). In either case the electronics amounts to frequency counting. As long as the laser exhibits sufficiently small timing noise at noise frequencies above $\Delta f_{\rm rep}/2$, the frequency counter's output corresponds to the true fluctuations in $\Delta f_{\rm rep}(t)$. This $\Delta f_{\rm rep}(t)$ can then be used to correct for the timing fluctuations in post-processing (resampling), or it can be used as a feedback signal on the laser to obtain few-femtosecond residual jitter [41].

The infrequent sampling of the time stamps (at a rate of $1/\langle \Delta f_{\rm rep} \rangle$) has significant implications in the context of

THz-TDS. The PCA output inevitably corresponds to a small photocurrent ($\sim\mu$A level), which calls for transimpedance amplification (TIA). The thermal noise contribution to the input-inferred current noise power spectral density favors operation with higher transimpedance gain, but TIAs are also subject to gain-bandwidth limitations. Therefore, a small $\Delta f_{\rm rep}$ is beneficial for the TIA step because the THz frequencies are downscaled by the factor $\Delta f_{\rm rep}/f_{\rm rep}$, meaning that a smaller RF bandwidth is needed to capture the THz features. However, with a free-running dual-comb we cannot make $\Delta f_{\rm rep}$ arbitrarily small because at some point there will be too much timing jitter noise above the sampling rate. Therefore, jitter is also important in the context of the dynamic range of the measurement.

Given the constraints of using IGMs to determine $\tau(t)$ it is worth noting alternative approaches. The phase $\phi_\Delta(t)$ can also be determined by measuring $\phi_f^j(t) = 2\pi \int f_{\rm rep}(t')dt'$ of each comb $j$ and taking the difference. The phases $\phi_f(t)$ can be obtained by detecting the pulse trains on high-speed photodiodes and filtering out a high harmonic; a powerful scheme for extracting $\Delta f_{\rm rep}$ by mixing each $f_{\rm rep}$ harmonic with a common RF oscillator was discussed in [51]. While this approach is less sensitive to laser timing jitter and can be used to electronically adjust $\phi_\Delta(t)$ [18], it requires a more complicated setup (e.g. a high-frequency RF oscillator, two high-speed photodiodes, mixers, filters, low-noise amplifiers, and digital phase analysis) to reach the few-femtosecond-level precision [52]. Therefore, here we focus on the direct $\Delta f_{\rm rep}$ measurement approach. In Section 3.B we detail the construction of the laser, with particular emphasis on features that relate to noise performance. In Section 3.C we study the laser's relative timing jitter (noise on $\Delta f_{\rm rep}$) and examine the implications for resampling of THz-TDS signals. In Section 4 we examine the contributing factors to the noise of $\Delta f_{\rm rep}$, how these are successfully mitigated by the design of the laser, and the broader implications for similar lasers.

### B. Low-Noise-Laser Configuration

In our previously published work we showed gigahertz dual-comb generation using a high-power spatially multimode pump diode. Here we demonstrate a complementary approach of modelocking in the 100 mW regime. We target this power because it is sufficient to drive the THz-PCAs, and because the lower power greatly relaxes cooling requirements. Consequently the laser is straightforward to passively cool, which in turn avoids mechanical noise from water cooling and opens up more options in terms of environmental isolation.

The laser setup is shown in Fig. 4. The laser is pumped by a 980 nm fiber Bragg grating (FBG) stabilized pump diode that delivers up to 960 mW of pump power from a single-mode fiber. Current is provided by a low-noise diode driver (Koheron CTL300E). A small part of the output power of the pump diode is split off with a polarization-maintaining 99:1 fiber splitter (Thorlabs PN980R1A1) in order to support (optional) feedback stabilization of the pump power; the maximum power from this port is about 10 mW. When the pump feedback loop is active, this beam is sent onto a 70 MHz reverse biased InGaAs photodiode, the output of which is used as the error
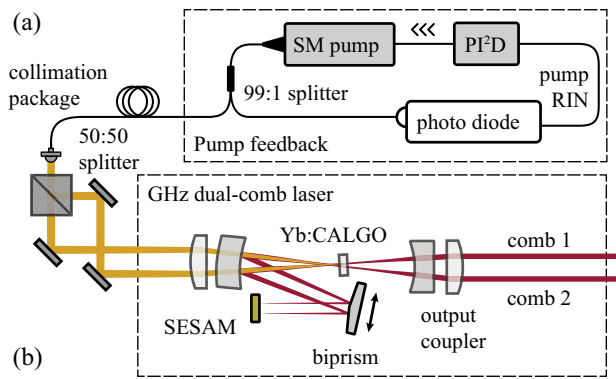
**Fig. 4.** Gigahertz dual-comb laser setup. (a) Pumping: the laser is pumped by a single-spatial-mode diode, with the option for feedback control on the pump power. (b) Cavity: the laser uses Yb:CALGO as gain medium and has a SESAM for modelocking. An intracavity biprism allows for generating two combs with slightly different $f_{rep}$ in the same cavity arrangement.

input signal to a $PI^2D$ servo (Vescent D2-125) acting on the current modulation of the laser diode driver. The main part of the pump power is collimated and routed in free space. To pump the two combs, the collimated beam is split into two equal parts with a non-polarization-dependent thin-film coating beam splitter. The two beam components are then recombined next to each other at a D-shaped mirror, as shown in Fig. 4. By using a shared pump, the pump-induced timing fluctuations are highly correlated (examined in Section 4).

The laser cavity layout is shown in Fig. 4(b). A reflective biprism (179° apex angle) is used to obtain dual-comb generation by spatial multiplexing of the cavity. The cavity design yields separate spots for the two combs on all of the active elements (gain crystal and SESAM), which is important for mitigating crosstalk. Note that the actual multiplexing of the cavity is implemented in the vertical for symmetry reasons, but is shown in Fig. 4 in the horizontal for simplicity. The cavity was carefully designed to support a confocal focusing arrangement as well as dual-comb generation, which is in contrast to the end-pumping arrangement of our previous dual-comb cavities [41,42,53]. Such a confocal arrangement supports tighter focusing in the gain medium and avoids high intensity on the dielectric mirrors. The beams are separated by 1.6 mm on the high-reflection (HR)-coated biprism, which allows for continuous tuning of the repetition rate difference in a range of [−175, 175] kHz by lateral translation of the biprism. By having the two combs share all the same optical components and stay within a few mm of each other throughout the cavity, mechanical and acoustic noise sources are highly correlated between the two combs.

The laser cavity is pumped through a convex-concave cavity turning mirror that has a radius of curvature (ROC) of −35 mm and a high transmission for the pump wavelength. Both pump beams are focused with a 50 mm focal length aspheric lens (Thorlabs AL2550M-B) onto two separate spots in the gain crystal. The crystal is a 1.5-mm-long 3% at. ytterbium-doped CALGO gain crystal (*a*-cut). The pump polarization is aligned along the crystal *c*-axis, while both combs are polarized along the *a*-axis of the crystal. The crystal is oriented such that this

corresponds to vertical (*s*-) polarization in the cavity in order to reduce the sensitivity of the mirror coatings to angle of incidence changes off from zero degree. Keeping the cavity group delay dispersion (GDD) symmetric between the two combs ensures a similar transfer function between laser relative intensity noise (RIN) and timing jitter, which helps keep timing fluctuations of the two combs correlated. The two co-polarized output beams are coupled out via the 0.8% transmission output coupler (ROC = −25 mm). Modelocking is initiated by a semiconductor saturable absorber mirror (SESAM) with a modulation depth of $\Delta R = 1.24\%$ and a fast recovery time of below 1 ps. Soliton formation is achieved by adding a total of $\approx -500\,\mathrm{fs}^2$ negative GDD by the intracavity mirrors (custom coating runs from Laseroptik GmbH). The nominal output properties of the laser were presented earlier in Fig. 2.

After accounting for the GDD of the gain material [54], we estimate a round-trip GDD of $\approx -210\,\mathrm{fs}^2$. This relatively small GDD mitigates timing jitter associated with intensity-dependent shifts in the laser center wavelength. To help quantify this source of noise, in Fig. 5 we examine the power dependence of the laser output. We obtain modelocked operation over an average output power range from about 80 mW to 110 mW per comb [Fig. 5(a)], limited by the available pump power. As expected for soliton modelocking, the pulse duration decreases with output power. At the same time, there is a noticeable shift in laser wavelength as a function of laser output power, with a slope of about +66 pm/mW for comb 2 [Fig. 5(b)]. The wavelength shifts can likely be attributed to the population inversion reducing as the laser goes further into its modelocking regime, resulting in the net intracavity spectral filter shifting to longer wavelengths due to the inversion dependence of the gain spectrum in the quasi-three-level gain medium. This behavior is even exhibited for Yb:YAG lasers despite their narrower gain bandwidth [55]. The implications of this effect are examined in Section 4.

## C. Relative Timing Jitter

Next we analyze the $\Delta f_{rep}$ noise properties of the laser. Fast fluctuations in $\Delta f_{rep}$ are the most critical issue as they lead to inaccuracies in Eq. (1). To quantify these fluctuations systematically, we characterize $\Delta f_{rep}$ by a method sufficient to achieve sub-femtosecond accuracy of the optical delay at all times in the measurement, independent of $\langle \Delta f_{rep} \rangle$. Our setup uses heterodyne beating between the two combs and a pair of narrow-linewidth single-frequency lasers (instantaneous optical linewidth <10 kHz), as described in detail in the context of noise measurements in [53]. Taking suitable differences between these beat notes yields a frequency $N\Delta f_{rep}$, where $N \sim 10^4$ is the number of optical comb lines between the two cw lasers. We calculate the phase noise power spectral density (PN-PSD) of $\phi_\Delta$ and use the fact that $2\pi$ change in phase corresponds to $1/f_{rep}$ in delay to scale it to a timing jitter (TJ)-PSD [56]. The resulting TJ-PSD is shown in Fig. 6. Three regimes can be observed: (i) a $1/f^2$ dependence for intermediate frequencies, (ii) a measurement-limited noise floor above 60 kHz, and (iii) additional "bumps" below 2 kHz attributable to mechanical/acoustic noise.
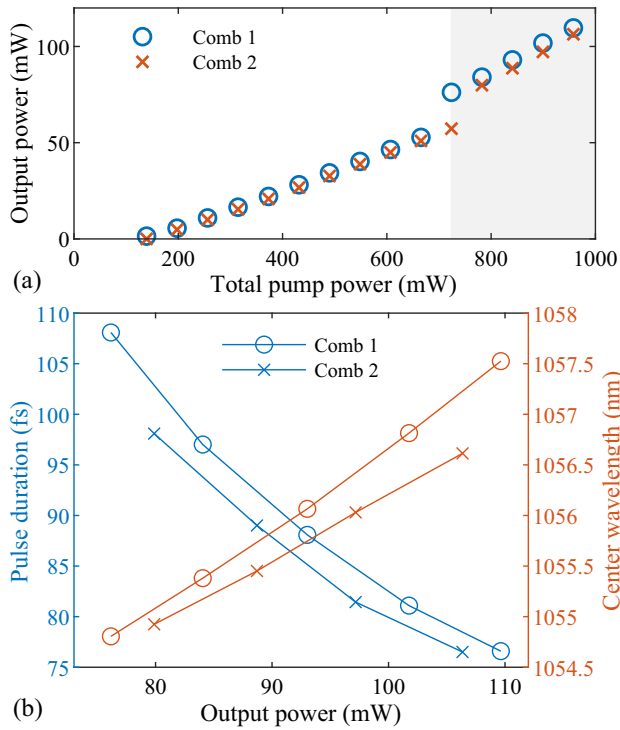
**Fig. 5.** (a) Laser output power versus pump power. A clear jump is observable when the laser enters the modelocking regime. (b) Pulse duration and center wavelength as a function of laser output power. The center was obtained from a center of mass calculation of the optical spectrum.
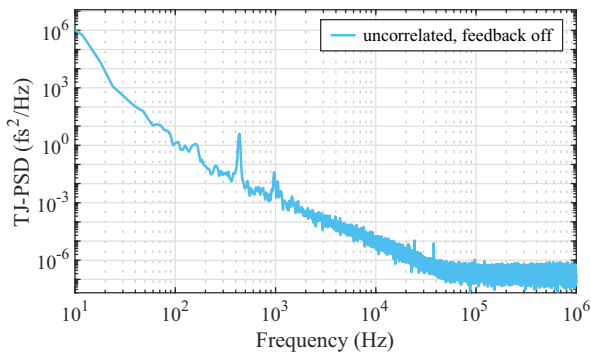


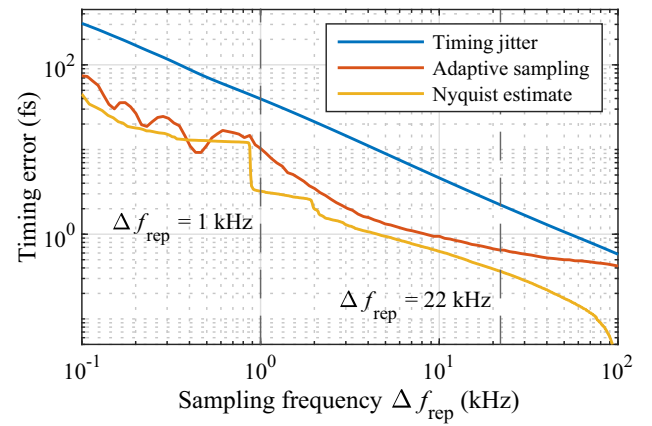**Fig. 7.** Timing error analysis. Blue (period jitter): direct period jitter measurement via the TJ-PSD of $\Delta f_{rep}(t)$. Red (resampling): RMS fluctuations between the true optical delay profile and the profile obtained by linear interpolation between the time stamps. Orange (Nyquist): RMS fluctuations inferred from Eq. (3).



**Fig. 6.** Timing jitter power spectral density (TJ-PSD) derived from fluctuations in $\Delta f_{rep}$.

We generally do not observe significant changes in the $\Delta f_{rep}$ TJ-PSD on the mean value $\langle \Delta f_{rep} \rangle$. However, the implications of the TJ-PSD are very dependent on $\langle \Delta f_{rep} \rangle$. When using the IGMs to infer the optical delay we only have access to aliased $\Delta f_{rep}$ data, so a perfect reconstruction is not possible. A straightforward yet slightly misleading estimate of the errors can be obtained from the period jitter, which corresponds to a $\sin^2$ weighted integral of the TJ-PSD [53,57]. The result is shown as the blue curve in Fig. 7. However, resampling can effectively suppress the influence of low-frequency-noise components that contribute to the period jitter. To simulate the efficacy of resampling for different values of $\langle \Delta f_{rep} \rangle$, we take a measured $\Delta f_{rep}(t)$ profile, calculate the IGM peaks $T_n$ that one would

obtain for different values of $\langle \Delta f_{rep} \rangle$, use those samples to linearly re-interpolate $\Delta f_{rep}(t)$, and calculate the root mean square (RMS) deviations between the true and interpolated $\Delta f_{rep}(t)$ arrays. The result is shown as the red curve in Fig. 7. An alternative interpolation approach is to make use of the sampling theorem, and examine the errors obtained if one were to reconstruct $\Delta f_{rep}$ under the (incorrect) assumption of noise being bandwidth-limited to the Nyquist range $\langle \Delta f_{rep} \rangle/2$. The resulting root mean square (rms) error can be estimated as

$$\mathrm{rms}\,[\tau]\,(\Delta f) \approx \sqrt{2 \int_{\Delta f/2}^{f_{max}} S_\tau(f)\mathrm{d}f}, \qquad (3)$$

where the factor of two comes from integrating two copies of the high-frequency-noise spectrum: one for noise on the true $\Delta f_{rep}$ array, the other for aliased replicas of the spectrum shifted within the Nyquist band on the interpolated $\Delta f_{rep}$ array. The result is shown in Fig. 7. There are clear similarities between the resampling method and the Nyquist estimate; we use the linear interpolation approach due to its simplicity. We find an RMS timing error of the optical delay axis of <1 fs for $\Delta f_{rep} = 18$ kHz and <10 fs for $\Delta f_{rep} = 1$ kHz. For the THz-TDS measurements we operate in two configurations: at $\Delta f_{rep} = 22$ kHz where low-frequency-noise sources have a negligible impact, and $\Delta f_{rep} = 1$ kHz where the timing error is still small compared the THz features, e.g., >200 fs cycle for a maximum THz frequency of 5 THz. As we will see later, operating at even lower $\Delta f_{rep}$ would be beneficial in terms of amplifier voltage noise, but Fig. 7 shows how this would lead to excessive jitter in our case due to low-frequency-technical-noise sources. These noise sources could be strongly mitigated by an optimized optomechanical setup, which was not available here (the current setup was constructed on an optical breadboard with standard mirror mounts and 5 cm high pedestals).
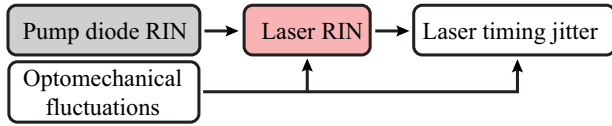
**Fig. 8.** Conceptual illustration of noise transfer in the laser.

## 4. SUPPRESSION OF TIMING JITTER

### A. Noise Sources

The low $\Delta f_{\mathrm{rep}}$ noise shown in Section 3.C is due to a combination of noise sources and correlation effects. In this section we examine these issues, how they can be improved, and determine practical operating constraints for ETS measurements such as THz-TDS. Timing jitter in our laser arises either directly from environmental sources, or from modelocking dynamics [58]. The latter includes intensity-dependent changes in the cavity round-trip time, which can originate either from pump intensity fluctuations or from environmental sources that couple to laser alignment. A conceptual illustration of this noise transfer is shown in Fig. 8. A convenient summary of several relevant sources is in [59,60], but we find that in these types of Yb-based DPSSLs the dominant contributions are environmental noise and power-dependent wavelength shifts that lead to round-trip time changes via the cavity GDD. Therefore, we approximate the TJ power spectral density (PSD) of each comb as

$$S_T(f) = H_T(f) S_{\mathrm{RIN}}(f) + S_T^{\mathrm{env}}(f), \qquad (4)$$

where $S_x$ indicates a one-sided power spectral density [56]. $S_T^{\mathrm{env}}$ is a generic term quantifying diverse environmental noise sources, and $H_T$ is a transfer function connecting intensity fluctuations to timing jitter given by

$$H_T(f) = \left(\frac{f_{\mathrm{rep}}\kappa}{2\pi f}\right)^2, \qquad (5)$$

where $\kappa = P(dT_{rt}/dP)$ is the normalized derivative of the cavity round-trip time $T_{rt}$ with respect to power $P$. We can express this coefficient in terms of laser parameters as

$$\kappa = \frac{dT_{rt}}{dP} P \approx -\beta_{\mathrm{GDD}} \frac{2\pi c}{\lambda_0^2} \frac{d\lambda_0}{dP} P, \qquad (6)$$

where $\lambda_0$ is the laser center wavelength. The wavelength shift is obtained from Fig. 5(b) and is approximately $d\lambda_0/dP = 65.8$ pm/mW for comb 2. Therefore, assuming $\beta_{\mathrm{GDD}} = -210$ fs$^2$, $\lambda_0 = 1056.7$ nm, and $P = 107$ mW we obtain $\kappa = 2.5$ fs. In a dual-comb laser with identical yet independent combs the noise spectrum is $S_\tau(f) = 2S_T(f)$, which implies that the available strategies to suppress noise are to decouple the cavity from the environment, reduce $\kappa$ by laser design, or reduce $S_{\mathrm{RIN}}$. Alternatively, one can introduce correlations between the timing jitter fluctuations of the two combs in order to yield $S_\tau(f) \ll 2S_T(f)$.

### B. Measurements

In Fig. 9 we compare the timing jitter noise associated with $\Delta f_{\mathrm{rep}}$ and the $f_{\mathrm{rep}}$ of each comb, and how these are influenced by pump intensity stabilization. The various features can be
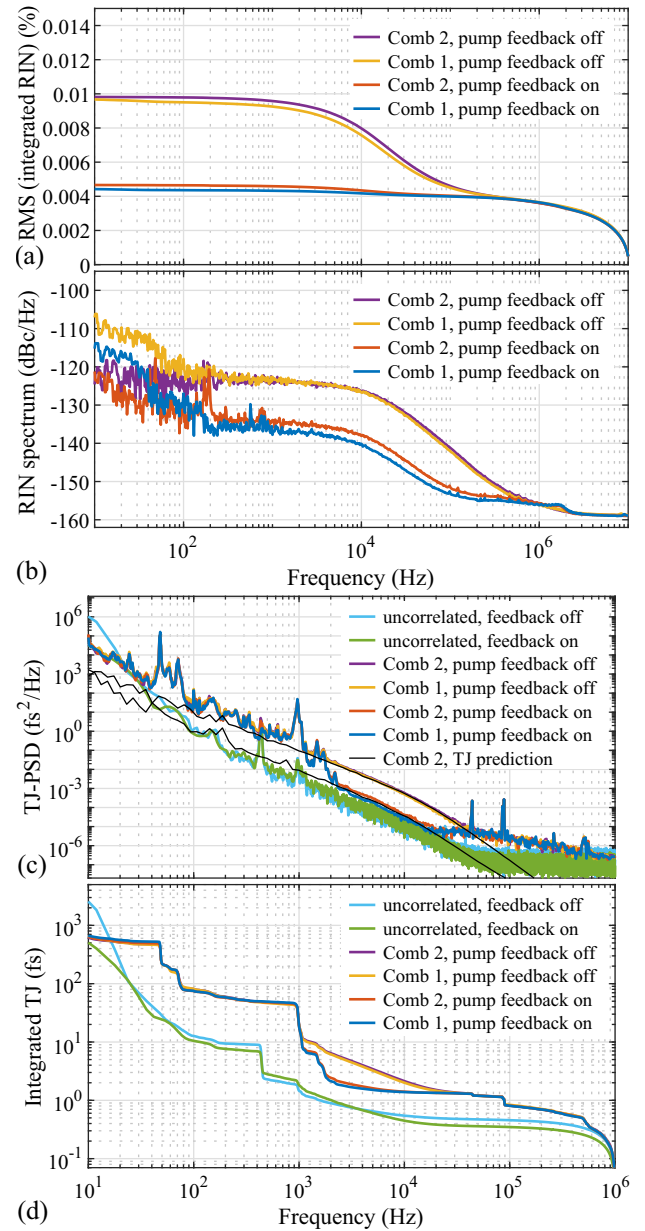


**Fig. 9.** Full noise characterization of the combs at the maximum output power of $\approx 110$ mW per comb. Results are shown with and without the pump power feedback loop. (a), (b) Relative intensity noise (RIN) characterization; (a) shows the integrated RIN, while (b) shows the one-sided RIN power spectral density. (c), (d) Timing jitter (TJ) characterization; (c) shows the one-sided TJ power spectral density, while (d) shows the integrated TJ. The jitter corresponding to $f_{\mathrm{rep}}$ of the individual combs as well as $\Delta f_{\mathrm{rep}}$ is shown. The black lines correspond to the predictions of Eq. (4) for comb 2 using the RIN spectrum from part (b). The upper and lower black curves are for pump feedback off and on, respectively; both show good agreement with the directly measured TJ-PSD curves.

explained with the help of the laser's relative intensity noise (RIN) power spectral density, which is shown in Figs. 9(a) and 9(b). The RIN is characterized by the same approach of [41] using baseband measurements on a signal source analyzer. For the free-running case (feedback off) the RIN exhibits typical features for Yb-based DPSSLs: a slight increase in noise at low

frequencies, a plateau at intermediate frequencies limited by the laser diode, a decay towards shot noise limited performance starting at ~20 kHz due to low-pass filtering by the gain medium, and an ultra-low integrated RIN <0.01%. By simply switching on the pump feedback loop [see Fig. 1(a)], the laser RIN-PSD is reduced by about 15 dB. The RIN-PSDs corresponding to the two cases (stabilization on/off) merge at around 500 kHz, and by this point the noise is already very low; there is an indication of a small servo bump from the pump feedback loop at $\approx 2$ MHz. The integrated RIN [Fig. 9(a)] is reduced by about a factor of two, resulting in similar values to the ultra-low RIN we reported for the 80 MHz dual-comb system in [41].

Given the RIN spectra of the two combs and the cavity delay coefficient $\kappa = 2.5$ fs from Eq. (6) we can predict the laser's TJ-PSD via Eq. (4). The result for comb 2 is shown by the black curve in Fig. 9(c) and is in excellent agreement with the directly measured timing jitter of the individual combs. This TJ-PSD was obtained by a standard measurement of the phase noise of an $f_{\mathrm{rep}}$ harmonic using a high-speed photodiode and a signal source analyzer. The measurement and theory are in good agreement for intermediate frequencies from 2 kHz to 40 kHz. At lower frequencies there are additional environmental noise sources corresponding to $S_T^{\mathrm{env}}$, while for frequencies beyond 40 kHz the TJ-PSD is likely measurement noise limited.

Further validation of the 2 kHz to 40 kHz noise being RIN-dominated can be seen by activating the pump feedback loop. With feedback active, the TJ-PSD decreases by about 13 dB, yielding corresponding improvements in the integrated TJ visible in Fig. 9(d). Interestingly, the $\Delta f_{\mathrm{rep}}$ noise spectrum is hardly affected by the pump feedback. This indicates that, with feedback switched off, the individual lasers' power fluctuations are already correlated to a greater extent than the noise-reduction caused by pump feedback. A possible explanation for why the $\Delta f_{\mathrm{rep}}$ noise is unaffected by pump RIN stabilization is the presence of asymmetric noise contributions, e.g., from the non-ideal polarization extinction ratio of the pump, or from noise contributions other than pump RIN. In any case, the results show that pump stabilization and pump sharing both yield significant improvements in RIN-related jitter, with the latter having slightly better performance ($>15$ dB) and yielding sufficiently low noise for our THz-TDS measurements. In the THz measurements we operate the laser without the pump feedback loop.

As well as pump-related noise, environmental noise in the [0.1, 2] kHz band is also important. The influence of the shared cavity can be seen for frequencies below 2 kHz, where noise spectrum reductions of 15 dB to 20 dB are apparent through most of the spectrum, except for an uncorrelated noise source around 440 Hz.

### C. Simplified Estimates

The timing error should be much smaller than the temporal features on the signal being measured. A reasonable criterion is that the timing error RMS should be less than about 5% to 10% of the inverse of the maximum THz frequency to be measured. In general this condition can be evaluated using Fig. 7 (or the related curves in Fig. 9); in this section we consider some simplified examples.

The low-frequency noise of Fig. 9 is not universal but rather limited by the mechanical details of the laser construction. Significant improvements to both $f_{\mathrm{rep}}$ and $\Delta f_{\mathrm{rep}}$ can be obtained by cavity assemblies with non-adjustable mirrors, examples of which have been presented in recent years [44,61]. It is therefore interesting to consider the RIN-dominated case and quantify the timing error. If we consider an oversimplified case where the power-dependent wavelength shift dominates and the RIN spectrum is frequency independent, we can obtain a convenient approximate expression for the timing error by substituting twice the value of $S_T(f)$ from Eq. (4) into Eq. (3). We obtain the following:

$$\mathrm{rms}\,[\tau]\,(\Delta f) \sim \frac{\kappa f_{\mathrm{rep}}}{\pi}\sqrt{\frac{\chi\,S_{\mathrm{RIN}}}{\Delta f_{\mathrm{rep}}}}, \tag{7}$$

where $\chi$ is a correlation parameter. For independent and identically distributed noise $\chi = 2$, while $\chi \to 0$ for fully correlated comb noise.

Evaluating this equation for $f_{\mathrm{rep}} = 1.18$ GHz, $\Delta f_{\mathrm{rep}} = 1$ kHz, $\kappa = 2.5$ fs, $S_{\mathrm{RIN}} = 0.5 \times 10^{-12}$ Hz, and $\chi = 2$ we obtain 29 fs, which would already start to be problematic as it is about 10% of the THz optical cycle (or even more for experiments targeting higher THz frequencies); for $\Delta f_{\mathrm{rep}} = 100$ Hz the jitter would certainly compromise the measurement. But, if $\chi = 10^{-2}$ (20 dB reduction in the $\Delta f_{\mathrm{rep}}$ noise spectrum compared to the $f_{\mathrm{rep}}$ spectrum), the calculation yields 21 fs even for $\Delta f_{\mathrm{rep}} = 10$ Hz, which would be sufficient for THz measurements up to $\sim 5$ THz. These calculations help show how a combination of the three methods we have explored (shared pumping, pump stabilization, and shared cavity architecture) can help enable operation at lower $\Delta f_{\mathrm{rep}}$ (with favorable implications for dynamic range) or access to higher THz frequencies from free-running dual-comb lasers.

### D. Laser Design Considerations

In [42] we presented a high-power gigahertz dual-comb source. The laser we present here has the same gain material (Yb:CALGO), a similar gigahertz repetition rate, and uses a similar spatial multiplexing scheme (reflective biprism here, Brewster-angled biprism in [42]). The present laser uses a lower output coupling rate to implement soliton modelocking at lower average power. The main difference between the two lasers is the pumping scheme and corresponding average power: here we use a lower power pump that is FBG-stabilized and delivered through a single-mode fiber (SM pump); in [42] we used a higher-power pump that was volume Bragg grating (VBG) stabilized and delivered through a multimode fiber (MM pump). It is interesting to compare the different approaches in the context of noise performance.

One might think that MM pumping inevitably leads to higher noise, but this is not the case. For example, in Fig. 4 of [41] we examined the RIN from a similar laser using an MM pump and operating at 80 MHz. The spectrum showed a "plateau" of around $-130$ dBc/Hz or slightly lower for frequencies between about 100 Hz to 1000 Hz. Direct measurements of the pump diode show a similar plateau extending to higher frequencies (usually slightly below $-130$ dBc/Hz). Similar

noise behavior has been observed in cw fiber lasers [62]. In comparison, the RIN-PSD from Fig. 9(b) shows a plateau at about −123 dBc/Hz, slightly less than 10 times higher and consistent with our direct characterization of the laser diode RIN (not shown). However, the pump power stabilization scheme brought the SM pumped laser to slightly lower noise than that obtained for MM pumping.

SM pump lasers are well suited to this kind of direct pump feedback. In MM pumped lasers we have found that direct feedback of the diode power does not reliably translate to reduction in modelocked laser RIN, possibly due to non-eliminated noise in the pump spatial profile. This indicates that reliable improvements require feedback directly on the modelocked laser power rather than the pump power in MM pumped lasers. While very feasible, this type of feedback is more complicated and constrained since it is subject to the dynamics of the modelocked laser, which includes the slow response of the Yb-doped gain medium.

Regarding the $1/f^2$ part of the $f_{rep}$ TJ noise, the TJ-PSD of [42] had a slightly lower noise power spectral density than what we have presented in Fig. 9, by about a factor of two. However, the $1/f^2$ part of the $\Delta f_{rep}$ noise spectrum is very similar between the two lasers because we obtain better correlation here. The improved correlation may be due to the absence of speckle in the pump laser beam due to SM pumping. With respect to low-frequency noise, SM pumped lasers have the advantage that they are easier to passively cool while maintaining isolation from environmental noise sources. Therefore, given the similar performance of the two lasers in terms of pulse duration, repetition rate, and high-frequency noise, the main motivation for SM pumping in this context is to obtain a laser that is matched to the application in terms of system-level considerations (potential size, weight, and power).

## 5. THZ-TDS DYNAMIC RANGE

Having established the repetition rate values accessible in our existing laser and given insights in what would be possible with optimized setups, we now examine the implications on THz-TDS dynamic range (DR). The THz-PCA devices we use are connected to a coaxial cable, which we interface with available commercial TIAs from Femto GmbH. The DR of the measurements is determined by the signal strength (discussed in Section 2.C) and the noise floor of the TIA. The accessible amplifier settings are constrained by the gain-bandwidth limitations of the commercial TIAs and by the jitter-related $\Delta f_{rep}$ limitations discussed in Sections 3 and 4.

### A. SNR

Figure 10 shows the THz spectrum and measurement noise background for two different $\Delta f_{rep}$ values: 22 kHz in Fig. 10(a) and 1 kHz in Fig. 10(b). For the high-update-rate case the scale factor between the THz and RF domains is $\approx 1.86 \times 10^{-5}$. Therefore, detection of THz frequencies up to 5 THz requires an RF bandwidth of 93 MHz; low-noise amplification of a weak signal with this high gain bandwidth is challenging. In our detection scheme we use a transimpedance amplifier with a 3 dB bandwidth of 200 MHz and a modest transimpedance
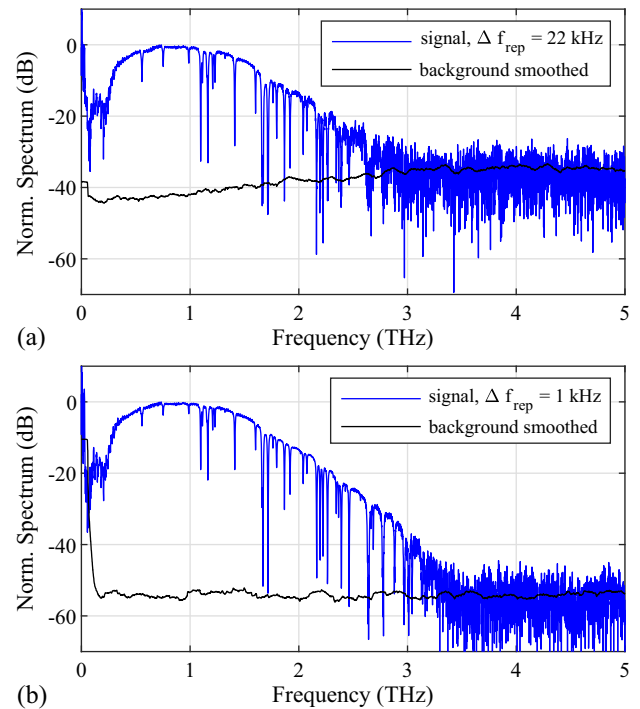


**Fig. 10.** THz-TDS spectra obtained from averaging 2-s-long traces. The spectra are obtained from Fourier transformation of time-domain THz signals with a 500 ps apodization window. (a) $\Delta f_{rep} = 22$ kHz, which yields a dynamic range of 35 dB. (b) $\Delta f_{rep} = 1$ kHz, which yields an improved dynamic range of 55 dB due to the improved amplifier noise floor. The background curves were obtained by taking a time trace with the free space THz beam path blocked and then smoothing the resulting spectrum. The clear absorption features stem from water absorption in the air path. Note that the absorption strength is changed due to different humidity conditions for the two measurements [late summer for (a) and early winter for (b)].

gain of $10^4$ V/A (Femto HCA S) followed by a broadband low-noise voltage amplifier (Femto DUPVA-1-70) with a voltage gain of 30 dB. Lastly, we use a 200 MHz anti-aliasing filter (Minicircuits BLP-200+) before digitalization with the oscilloscope (Lecroy WavePro 254HD). The TIA has a relatively high equivalent input noise floor of 4900 fA/$\sqrt{\text{Hz}}$.

For the 1 kHz case the required amplification bandwidth is significantly relaxed: an RF bandwidth of $\approx 4.2$ MHz is needed for THz frequencies up to 5 THz. Therefore, for this measurement we replace the HCA-S amplifier with a DHPCA-100 amplifier (FEMTO), which (for the setting used) has a transimpedance gain $10^5$ V/A, a bandwidth of 3.5 MHz, and an input equivalent noise current of 480 fA/$\sqrt{\text{Hz}}$. As expected from the square ratio of the noise floors, we obtain an improvement in 20 dB in the DR of the THz spectrum [Fig. 10(b)]. For comparison purposes, it is useful to normalize our results to the general dependence of DR on the measured time window $T_{range}$ and integration time $T_{meas}$. Therefore we define a normalized DR as

$$R_{norm} = (DR) \frac{T_{range}^2}{T_{meas}}. \tag{8}$$

The 500 ps apodization window discussed in Section 2.C is included before taking the Fourier transform. Therefore, the

effective temporal range leading to the spectrum in Fig. 10 is 500 ps and the effective measurement time is the fraction of time spent within that delay range, i.e., 1.18 s. Therefore we can infer a normalized DR of $R_{norm} \approx 7 \times 10^2$ ns$^2$/s for the 22 kHz case and $R_{norm} \approx 7 \times 10^4$ ns$^2$/s for the 1 kHz case.

Although our signal strength is comparable to reference measurements (as discussed in Section 2.C), the reference measurements yielded a significantly higher DR. Specifically, a DR of 100 dB in the THz power spectrum was obtained when measuring an optical delay range of 70 ps and a total integration time of 60 s, similar to the results of [7]. This corresponds to a normalized DR of $R_{norm} \approx 10^6$ ns$^2$/s, which is a more directly comparable value than the DR since it accounts for the lower integration time and larger delay range of our measurement.

Nonetheless, the normalized DR of the reference measurement is still substantially higher. The discrepancy can be explained by the amplifier: in [7] the delay was obtained by a mechanical delay line, which implies a slow delay scan rate. Because of the slow delay scanning, THz features are stretched out more in the time domain, allowing for a transimpedance amplifier with a few tens of kHz bandwidth to be used instead. Under these conditions, the input equivalent noise current of low-noise transimpedance amplifiers such as the FEMTO DLPCA-200 can be as low as 43 fA/$\sqrt{\text{Hz}}$ for a transimpedance gain of $10^7$ V/A, yielding a 20 dB reduction in noise power compared to the DHPCA-100 settings in our 1 kHz measurement. If this additional factor could be removed by using a different amplifier, our normalized DR would be comparable to or even higher than that of [7]. While these calculations explain the main effects, it should be noted that the dynamic range can also be limited by the receiver antenna itself, so further improvements to the amplifier would have to be tested experimentally.

Similar amplifier settings would be accessible in our case with $\Delta f_{rep} = 10$ Hz. However, then the timing jitter error would be too large, especially because of the mechanical noise sources that bring the TJ-PSD above the $1/f^2$ trend in Fig. 9; this would preclude averaging of the full delay window with IGM-based resampling. Therefore, we restricted our measurements to the >1 kHz regime. With an optimized mechanical construction and well-correlated RIN-induced noise sources, high-quality measurements at ≪ 1 kHz should be possible according to the calculations of Section 4.C. Of course, it will not always be advantageous to operate at low $\Delta f_{rep}$ since some applications require kHz update rates, and access to such high update rates is an advantage of a dual-comb-based approach to ETS.

### B. Water Vapor Spectroscopy

Lastly, we examine the sharp absorption features that are clearly resolved in the spectra of Fig. 10. For both configurations ($\Delta f_{rep} = 22$ kHz and $\Delta f_{rep} = 1$ kHz) the THz spectra show identical sharp absorption peaks that can be identified as water absorption. To resolve these sharp absorption features as well as possible, for the analysis of this section we switch off the apodization window and use the full time range.

To infer the absorption spectrum from the measured THz spectrum we need to subtract the measured spectrum from its envelope. Since purging of the free-space THz path to 0%

relative humidity to obtain a reference spectrum is experimentally challenging, we instead extract the envelope of the THz spectrum from the THz time trace itself. To accomplish this, we estimate the absorption using the HITRAN database [63], add a complex spectral phase to obtain a causal filter, and divide the measured spectrum by the filter. This removes most of the absorption features from the spectrum and yields a nearly compressed pulse in the time domain. To avoid numerical instabilities, we restrict the correction to THz frequencies below 3.5 THz and HITRAN predicted absorption features with a strength of >1%. The resulting signal is then inverse Fourier transformed, apodized in the time domain with a 10 ps window, and Fourier transformed to obtain an envelope that is free of any rapidly varying spectral features. The measured spectrum is divided by the envelope spectrum to determine the absorption values.

Figure 11 shows the comparison of the resulting absorption peaks for the $\Delta f_{rep} = 1$ kHz case with a prediction from HITRAN. The good agreement for the measured position and relative strength of the absorption peaks with HITRAN indicates a well-calibrated and linear optical delay axis in our free-running dual-comb THz measurements.

## 6. DISCUSSION AND CONCLUSION

We have demonstrated THz-TDS with a new dual-comb laser platform and quantified the noise considerations in detail. The laser demonstrates a compelling combination of features for the first time: an Yb:CALGO gain medium, a spatially multiplexed dual-comb cavity, GHz repetition rate, and single-spatial-mode diode pumping. The confocal cavity design with a biprism operated in reflective configuration allowed for a wide tunability of the repetition rate difference up to ±175 kHz and pulse durations of 77 fs with 110 mW average power per comb. We studied the laser's noise properties, showing ultra-low-noise performance of $\Delta f_{rep}$ with a corresponding integrated timing jitter of ≈ 2.6 fs for a lower integration limit of 1 kHz. We examined two complementary strategies to reach noise at this level: either by shared pumping or modification of the laser diode driver to include active pump power control. While both approaches are beneficial, the benefits did not stack, so we relied purely on the shared pumping approach for THz measurements. It was also critical to use the shared cavity architecture supported by spatial multiplexing in order to avoid transfer of environmental noise sources below 2 kHz to $\Delta f_{rep}$ fluctuations. The noise of $f_{rep}$ with and without stabilization is very well explained by theory [Eq. (4)], which should be useful for optimizing different aspects of laser noise.

Our THz results show for the first time that gigahertz Yb lasers paired with Fe-doped PCA devices can already reach similar signal strengths to reference measurements at 1550 nm even though the devices were not designed for our laser wavelength. The pulse energies involved were well below those involved in 80 MHz reference measurements. For these reasons, Yb-based lasers represent a significant opportunity to scale the THz signal strength through optimized devices or scaling up laser power. For example, a factor of two in power scaling could be obtained straightforwardly by using two separate pump diodes. While the pump-noise correlations evident in Fig. 9(c) would not occur in
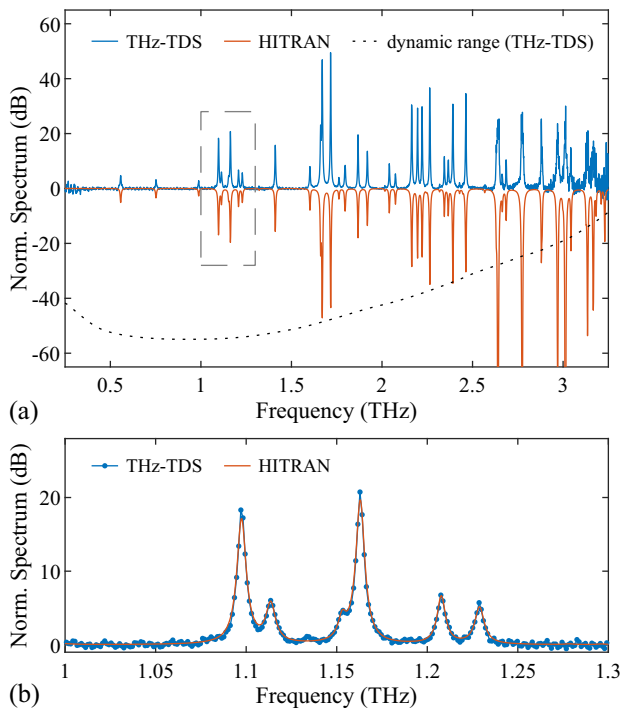
**Fig. 11.** (a) Comparison of the absorption features from an ≈30 cm free-space air path measured via THz-TDS and the prediction from HITRAN for a water ($H_2O$) vapor concentration of 1.1%. The THz-TDS absorption spectrum is obtained from the transmission spectrum via subtraction of the THz-spectrum envelope (see text). The positions of the absorption peaks are in excellent agreement. For high frequencies, the absorption strength deviates when the predicted peak absorption strength exceeds the dynamic range of the THz-TDS measurement, as indicated by the dashed line. (b) Zoom to the region between 1 THz and 1.3 THz to illustrate the spectral resolution of ≈1.2 GHz in the THz-TDS measurement, which samples well the individual absorption peaks. The THz-TDS measurement was obtained at a repetition rate difference $\Delta f_{rep} = 1$ kHz with a total integration time of 2 s.

that case, the power stabilization strategy we have shown would still be almost as effective.

More generally, the connection between laser timing noise and transimpedance amplifier current noise represents an important design trade-off to make most use of gigahertz-laser-based ETS. In our experiments we were limited to the parameters available from commercial transimpedance amplifiers, but improvements would likely be possible by optimized amplifier design, especially if the amplifier is integrated with the PCA device without a coaxial cable. Further repetition rate scaling could also alleviate the amplifier noise issue since the factor $\Delta f_{rep}/f_{rep}$ becomes smaller for a given measurement update rate, allowing for reduced amplifier bandwidth and therefore lower noise. This regime may require using the PCAs at lower energy but higher power (which would need to be tested), and may require further optimizations of timing jitter due to the $f_{rep}$ factor evident in Eq. (3). Overall, we anticipate this platform of low-complexity single-cavity solid-state dual-comb lasers at high repetition rates with excellent free-running timing noise performance to significantly benefit high-performance THz-TDS experiments, especially when considering the repetition

rate scalability towards 10 GHz [45] and the use of power-scalable Yb-doped gain media [42]. Our results are relevant for spectroscopy and metrology measurements in diverse scientific and industrial application areas, especially those requiring high update rates and high resolution.

**Disclosures.** The authors declare no conflicts of interest.

**Data availability.** The data that support the findings of this study are available from the corresponding author upon reasonable request.

## REFERENCES

1. M. Naftaly, N. Vieweg, and A. Deninger, "Industrial applications of terahertz sensing: state of play," Sensors **19**, 4203 (2019).
2. A. G. Davies, A. D. Burnett, W. Fan, *et al.*, "Terahertz spectroscopy of explosives and drugs," Mater. Today **11**, 18–26 (2008).
3. M. Yahyapour, A. Jahn, K. Dutzi, *et al.*, "Fastest thickness measurements with a terahertz time-domain system based on electronically controlled optical sampling," Appl. Sci. **9**, 1283 (2019).
4. E. Pickwell and V. P. Wallace, "Biomedical applications of terahertz technology," J. Phys. D **39**, R301–R310 (2006).
5. M. van Exter, C. Fattinger, and D. Grischkowsky, "Terahertz time-domain spectroscopy of water vapor," Opt. Lett. **14**, 1128–1130 (1989).
6. D. R. Bacon, J. Madéo, and K. M. Dani, "Photoconductive emitters for pulsed terahertz generation," J. Opt. **23**, 064001 (2021).
7. B. Globisch, R. J. B. Dietz, R. B. Kohlhaas, *et al.*, "Iron doped InGaAs: competitive THz emitters and detectors fabricated from the same photoconductor," J. Appl. Phys. **121**, 053102 (2017).
8. R. B. Kohlhaas, S. Breuer, S. Nellen, *et al.*, "Photoconductive terahertz detectors with 105 dB peak dynamic range made of rhodium doped InGaAs," Appl. Phys. Lett. **114**, 221103 (2019).
9. R. B. Kohlhaas, S. Breuer, L. Liebermeister, *et al.*, "637 µW emitted terahertz power from photoconductive antennas based on rhodium doped InGaAs," Appl. Phys. Lett. **117**, 131105 (2020).
10. U. Puc, T. Bach, P. Günter, *et al.*, "Ultra-broadband and high-dynamic-range THz time-domain spectroscopy system based on organic crystal emitter and detector in transmission and reflection geometry," Adv. Photon. Res. **2**, 2000098 (2021).
11. S. Mansourzadeh, T. Vogel, A. Omar, *et al.*, "Broadband THz-TDS with 5.6 mW average power at 540 kHz using organic crystal BNA," arXiv, arXiv:2209.08876 (2022).
12. N. Hoghooghi, S. Xing, P. Chang, *et al.*, "Broadband 1-GHz mid-infrared frequency comb," Light Sci. Appl. **11**, 264 (2022).
13. O. Kara, L. Maidment, T. Gardiner, *et al.*, "Dual-comb spectroscopy in the spectral fingerprint region using OPGaP optical parametric oscillators," Opt. Express **25**, 32713–32721 (2017).
14. S. Vasilyev, A. Muraviev, D. Konnov, *et al.*, "Video-rate broadband longwave IR dual-comb spectroscopy with 240,000 comb-mode resolved data points," arXiv, arXiv:2210.07421 (2022).
15. K. Weingarten, M. Rodwel, and D. Bloom, "Picosecond optical sampling of GaAs integrated circuits," IEEE J. Quantum Electron. **24**, 198–220 (1988).
16. P. A. Elzinga, R. J. Kneisler, F. E. Lytle, *et al.*, "Pump/probe method for fast analysis of visible spectral signatures utilizing asynchronous optical sampling," Appl. Opt. **26**, 4303–4309 (1987).
17. D. Saeedkia, ed., *Handbook of Terahertz Technology for Imaging, Sensing and Communications*, Woodhead Publishing Series in Electronic and Optical Materials (Woodhead, 2013).

18. F. Tauser, C. Rausch, J. H. Posthumus, *et al.*, "Electronically controlled optical sampling using 100 MHz repetition rate fiber lasers," Proc. SPIE **6881**, 68810O (2008).

19. T. Hochrein, R. Wilk, M. Mei, *et al.*, "Optical sampling by laser cavity tuning," Opt. Express **18**, 1613–1617 (2010).

20. M. Kolano, B. Gräf, S. Weber, *et al.*, "Single-laser polarization-controlled optical sampling system for THz-TDS," Opt. Lett. **43**, 1351–1354 (2018).

21. A. Bartels, R. Cerna, C. Kistner, *et al.*, "Ultrafast time-domain spectroscopy based on high-speed asynchronous optical sampling," Rev. Sci. Instrum. **78**, 035107 (2007).

22. O. Kliebisch, D. C. Heinecke, and T. Dekorsy, "Ultrafast time-domain spectroscopy system using 10 GHz asynchronous optical sampling with 100 kHz scan rate," Opt. Express **24**, 29930–29940 (2016).

23. K. Gürel, V. J. Wittwer, M. Hoffmann, *et al.*, "Green-diode-pumped femtosecond Ti:sapphire laser with up to 450 mW average power," Opt. Express **23**, 30043–30048 (2015).

24. S. Backus, M. Kirchner, C. Durfee, *et al.*, "Direct diode-pumped Kerr lens 13 fs Ti:sapphire ultrafast oscillator using a single blue laser diode," Opt. Express **25**, 12469–12477 (2017).

25. H. Ostapenko, T. Mitchell, P. Castro-Marin, *et al.*, "Three-element, self-starting Kerr-lens-modelocked 1-GHz Ti:sapphire oscillator pumped by a single laser diode," Opt. Express **30**, 39624–39630 (2022).

26. Y. Wang, J. A. Holguín-Lerma, M. Vezzoli, *et al.*, "Photonic-circuit-integrated titanium:sapphire laser," Nat. Photonics **17**, 338–345 (2023).

27. T. Fortier and E. Baumann, "20 years of developments in optical frequency comb technology and applications," Commun. Phys. **2**, 1–16 (2019).

28. S. Schiller, "Spectrometry with frequency combs," Opt. Lett. **27**, 766–768 (2002).

29. I. Coddington, N. Newbury, and W. Swann, "Dual-comb spectroscopy," Optica **3**, 414–426 (2016).

30. S. M. Link, A. Klenner, M. Mangold, *et al.*, "Dual-comb modelocked laser," Opt. Express **23**, 5521–5531 (2015).

31. T. Ideguchi, T. Nakamura, Y. Kobayashi, *et al.*, "Kerr-lens mode-locked bidirectional dual-comb ring laser for broadband dual-comb spectroscopy," Optica **3**, 748–753 (2016).

32. S. Mehravar, R. A. Norwood, N. Peyghambarian, *et al.*, "Real-time dual-comb spectroscopy with a free-running bidirectionally mode-locked fiber laser," Appl. Phys. Lett. **108**, 231104 (2016).

33. N. Prakash, S.-W. Huang, and B. Li, "Relative timing jitter in a counterpropagating all-normal dispersion dual-comb fiber laser," Optica **9**, 717–723 (2022).

34. N. B. Hébert, J. Genest, J.-D. Deschênes, *et al.*, "Self-corrected chip-based dual-comb spectrometer," Opt. Express **25**, 8168–8179 (2017).

35. C. Zhang, F. Qu, P. Ou, *et al.*, "Recent advances and outlook in single-cavity dual comb lasers," Photonics **10**, 221 (2023).

36. R. D. Baker, N. T. Yardimci, Y.-H. Ou, *et al.*, "Self-triggered asynchronous optical sampling terahertz spectroscopy using a bidirectional mode-locked fiber laser," Sci. Rep. **8**, 14802 (2018).

37. G. Hu, T. Mizuguchi, R. Oe, *et al.*, "Dual terahertz comb spectroscopy with a single free-running fibre laser," Sci. Rep. **8**, 11155 (2018).

38. J. Chen, K. Nitta, X. Zhao, *et al.*, "Adaptive-sampling near-Doppler-limited terahertz dual-comb spectroscopy with a free-running single-cavity fiber laser," Adv. Photon. **2**, 036004 (2020).

39. B. Willenberg, J. Pupeikis, L. M. Krüger, *et al.*, "Femtosecond dual-comb Yb:CaF$_2$ laser from a single free-running polarization-multiplexed cavity for optical sampling applications," Opt. Express **28**, 30275–30288 (2020).

40. S. L. Camenzind, T. Sevim, B. Willenberg, *et al.*, "Free-running Yb:KYW dual-comb oscillator in a MOPA architecture," Opt. Express **31**, 6633–6648 (2023).

41. J. Pupeikis, B. Willenberg, S. L. Camenzind, *et al.*, "Spatially multiplexed single-cavity dual-comb laser," Optica **9**, 713–716 (2022).

42. C. R. Phillips, B. Willenberg, A. Nussbaum-Lapping, *et al.*, "Coherently averaged dual-comb spectroscopy with a low-noise and high-power free-running gigahertz dual-comb laser," Opt. Express **31**, 7103–7119 (2023).

43. S. Schilt, N. Bucalovic, V. Dolgovskiy, *et al.*, "Fully stabilized optical frequency comb with sub-radian CEO phase noise from a SESAM-modelocked 1.5-μm solid-state laser," Opt. Express **19**, 24171–24181 (2011).

44. T. D. Shoji, W. Xie, K. L. Silverman, *et al.*, "Ultra-low-noise monolithic mode-locked solid-state laser," Optica **3**, 995–998 (2016).

45. A. S. Mayer, C. R. Phillips, and U. Keller, "Watt-level 10-gigahertz solid-state laser enabled by self-defocusing nonlinearities in an aperiodically poled crystal," Nat. Commun. **8**, 1673 (2017).

46. S. Kimura, S. Tani, and Y. Kobayashi, "Kerr-lens mode locking above a 20 GHz repetition rate," Optica **6**, 532–533 (2019).

47. M. Hamrouni, F. Labaye, N. Modsching, *et al.*, "Efficient high-power sub-50-fs gigahertz repetition rate diode-pumped solid-state laser," Opt. Express **30**, 30012–30019 (2022).

48. H. Haus and A. Mecozzi, "Noise of mode-locked lasers," IEEE J. Quantum Electron. **29**, 983–996 (1993).

49. R. Paschotta, A. Schlatter, S. Zeller, *et al.*, "Optical phase noise and carrier-envelope offset noise of mode-locked lasers," Appl. Phys. B **82**, 265–273 (2006).

50. L. Antonucci, X. Solinas, A. Bonvalet, *et al.*, "Electronic measurement of femtosecond time delays for arbitrary-detuning asynchronous optical sampling," Opt. Express **28**, 18251–18260 (2020).

51. R. Paschotta, B. Rudin, A. Schlatter, *et al.*, "Relative timing jitter measurements with an indirect phase comparison method," Appl. Phys. B **80**, 185–192 (2005).

52. T. M. Fortier, F. Quinlan, A. Hati, *et al.*, "Photonic microwave generation with high-power photodiodes," Opt. Lett. **38**, 1712–1714 (2013).

53. S. L. Camenzind, D. Koenen, B. Willenberg, *et al.*, "Timing jitter characterization of free-running dual-comb laser with sub-attosecond resolution using optical heterodyne detection," Opt. Express **30**, 5075–5094 (2022).

54. P. Loiko, P. Becker, L. Bohatý, *et al.*, "Sellmeier equations, group velocity dispersion, and thermo-optic dispersion formulas for CaLnAlO$_4$ (Ln = Y, Gd) laser host crystals," Opt. Lett. **42**, 2275–2278 (2017).

55. M. Seidel, J. Pilat, L. Lang, *et al.*, "Ultrafast Yb:YAG laser oscillator with gigahertz repetition rate," Opt. Express **31**, 34313–34324 (2023).

56. I. S. C. C. 27, "IEEE standard definitions of physical quantities for fundamental frequency and time metrology–random instabilities," IEEE Std 1139-2008 (Revision of IEEE Std 1139-1999) (2009), pp. 1–50.

57. S. Meninger, "Phase noise and jitter," in *Clocking in Modern VLSI Systems*, Integrated Circuits and Systems, T. Xanthopoulos, ed. (Springer, 2009), pp. 139–181.

58. R. Paschotta, "Noise of mode-locked lasers (Part II): timing jitter and other fluctuations," Appl. Phys. B **79**, 163–173 (2004).

59. M. Endo, T. D. Shoji, and T. R. Schibli, "Ultralow noise optical frequency combs," IEEE J. Sel. Top. Quantum Electron. **24**, 1–13 (2018).

60. J. Kim and Y. Song, "Ultralow-noise mode-locked fiber lasers and frequency combs: principles, status, and applications," Adv. Opt. Photon. **8**, 465–540 (2016).

61. H. Ostapenko, Y. Feng, T. Lamour, *et al.*, "Misalignment-free, Kerr-lens-modelocked Yb:Y$_2$O$_3$ 2.2-GHz oscillator, amplified by a semiconductor optical amplifier," Opt. Express **31**, 3249–3257 (2023).

62. J. Zhao, G. Guiraud, C. Pierre, *et al.*, "High-power all-fiber ultra-low noise laser," Appl. Phys. B **124**, 114 (2018).

63. R. V. Kochanov, I. E. Gordon, L. S. Rothman, *et al.*, "HITRAN application programming interface (HAPI): a comprehensive approach to working with spectroscopic data," J. Quant. Spectrosc. Radiat. Transfer **177**, 15–30 (2016).